NORMAL IMPACT OF AN INFINITE ELASTIC–PLASTIC BEAM BY A SEMI-INFINITE ELASTIC ROD†

S. Ranganath‡ and R. J. Clifton§

Division of Engineering, Brown University, Providence, Rhode Island 02912

Abstract—Solutions are obtained for the problem of normal impact of an infinite elastic–plastic beam by a semi-infinite elastic rod. The effects of rotatory inertia and shear deformations are included in the equations governing the motion of the beam. A strain rate independent model based on concepts similar to those employed in quasi-static plasticity is used to describe material behavior. The interaction between moment and shear force is included. A strain hardening criterion is used based on the quasi-static moment–curvature relation for pure bending. Strain–time profiles computed using this theory agree reasonably well with those obtained in experiments on aluminum beams. The computed solutions are also compared with predictions based on a rigid perfectly plastic beam theory.

1. INTRODUCTION

THE response of structural systems to dynamic loading of sufficient intensity to produce plastic deformation is a subject of considerable technical importance. Structural elements such as beams and plates are often subjected to impact loading which produces flexural waves. Although considerable work has been done in the field of elastic waves in bending, few attempts have been made to study flexural waves in the plastic range. The study of plastic bending waves is more complex than that of plastic longitudinal waves because bending waves involve geometric dispersion and also combined stresses. The need to deal with stress resultants such as moment and shear force rather than the stresses themselves makes plastic bending waves inherently less amenable to analysis than is the case for other examples of combined stress plastic wave propagation such as that of combined longitudinal and torsional plastic waves.

Some of the difficulties associated with the analysis of plastic bending waves have been avoided in previous investigations by using Bernoulli–Euler beam theory, assuming a rigid, perfectly plastic characterization of the moment curvature relation, and neglecting the effect of the shear force on the value of the full plastic moment. The use of Bernoulli–Euler beam theory neglects the effects of rotatory inertia and shear deformation and leads to equations of parabolic type for which discontinuities in the solution are propagated at infinite speeds as is the case for solutions of the heat equation. If the equations are modified so as to include the effects of rotatory inertia and shear deformation as in the Timoshenko beam theory, then the system of equations becomes hyperbolic and discontinuities are propagated along characteristics at finite speeds. The assumption that the material is rigid, perfectly plastic neglects elastic deformation, strain hardening and the effects of

strain rate sensitivity. This assumption leads to major simplifications in the analysis of dynamic problems.

Considerable work has been done on comparisons of experimental results with predictions based on the rigid, perfectly plastic theory. Parkes [1–3], Bodner and Symonds [4, 5] and Florence and Firth [6] obtained the final deflection and rotation of beams experimentally, by subjecting beam specimens made of mild steel and aluminum alloys to transverse impact. The general conclusion from their studies was that the application of rigid, perfectly plastic analysis predicted final deformations almost twice as large as the experimental values in all the cases. Parkes, and Bodner and Symonds explained these discrepancies as being due to neglect of strain rate effects in the rigid plastic analysis. This explanation appears to be questionable for the case of tests on specimens made of 6061-T6 aluminum alloy since uniaxial stress–strain data [7] on this alloy shows very little dependence on strain rate. Besides, Florence and Firth concluded from their work that the discrepancies between the predicted and observed deformation magnitudes stem from the secondary effects like neglect of strain hardening and elastic deformations. Thus, there is need for further study of the problem in order to fully distinguish the roles of strain rate sensitivity, elastic deformation, strain hardening and plastic shear deformation. A critical review of these experiments is given by Symonds in his survey reports [8, 9].

Bohnenblust [10] solved the problem of constant velocity impact of a long elastic plastic beam using Bernoulli–Euler beam theory. Although this problem is in some respects artificial and impractical, Bohnenblust's solution is significant because it is the only complete and "exact" solution (consistent with the use of Bernoulli–Euler beam theory) of an impact problem for elastic–plastic beams. The predictions from the elastic theory were investigated experimentally by Vigness [11]. The strain at the impact point was predicted with reasonable accuracy by the Bohnenblust analysis. However, the assumed boundary condition of a step-function time dependence for the transverse velocity at the midpoint is difficult to realize exactly in the laboratory and exact agreement should not be expected. Apart from difficulties associated with the boundary condition, the analysis based on Bernoulli–Euler beam theory cannot be expected to be realistic at early times and near the wavefront as the effective wavelengths are comparable to the beam thickness. At the point of impact the predicted shear force is infinite initially; also, three dimensional effects are important in the neighborhood of the concentrated load. A more exact solution would require the use of the Timoshenko beam theory which includes the effects of rotatory inertia and shear deformations. Conroy [12] used the Bohnenblust analysis to solve the problem of constant velocity impact of infinite rigid plastic beams. He showed that for rigid, perfectly plastic beams the deformation is characterized by a fixed plastic hinge at the point of impact and a travelling plastic hinge.

Wilshaw and Kelly [13] investigated experimentally the response of a clamped circular plate to a rectangular stress pulse. They found that the elastic response of the plate was predicted well by classical thin plate theory. The plastic behavior was analyzed by assuming the material to be rigid visco-plastic and the predicted value of the final deflection was shown to be in substantial agreement with the experimental data.

We present here an investigation of the problem of normal impact of an infinite elastic–plastic beam of rectangular cross-section by a semi-infinite elastic rod. The effects of rotatory inertia and shear deformations are included in the equations governing the motion of the beam. A strain rate independent model based on concepts similar to those employed in quasi-static plasticity is used to describe the material behavior. The interaction between

moment and shear force is included. A strain hardening criterion is used which is based on the quasi-static moment–curvature relation for pure bending. The predicted strain response of the theoretical model is compared with the experimental strain response at different positions on the beam and for different velocities of impact.

2. EQUATIONS OF MOTION AND THE PROBLEM

The experimental set-up and the loading condition are similar to those described in [14, 15] except that here the impact velocity V_0 can be large enough to cause plastic deformation in the beam. Although plastic deformation occurs we assume that deformations are sufficiently small so that the assumption of infinitesimal strains and small deflections is applicable.

The equations of motion are the same as in the elastic case [14]. Thus,

$$Q + M_x = \rho I \psi_{tt} \tag{2.1a}$$

$$\mu \eta_{tt} = Q_x \tag{2.1b}$$

where
$\quad x$ = distance from the center of the beam where impact occurs;
$\quad t$ = time from the instant impact occurs;
$\quad M$ = bending moment;
$\quad Q$ = shear force;
$\quad \eta$ = transverse displacement;
$\quad \psi$ = angular rotation of the cross section of the beam;
$\quad \rho$ = mass density of the material of the beam;
$\quad I$ = moment of inertia of the cross section;
$\quad \mu$ = mass per unit length of the beam.

The relations between the generalized displacements η and ψ and the generalized strains γ and κ are

$$\eta_x - \psi = \gamma \tag{2.2a}$$

$$\psi_x = \kappa \tag{2.2b}$$

where
$\quad \gamma$ = shear strain;
$\quad \kappa$ = curvature.

The generalized strain rates κ_t and γ_t are assumed to be the sum of an elastic part and a plastic part. Thus we obtain,

$$\kappa_t = \kappa_t^e + \kappa_t^p \tag{2.3a}$$

$$\gamma_t = \gamma_t^e + \gamma_t^p \tag{2.3b}$$

where the superscripts e and p refer to the elastic and plastic parts, respectively.

For an elastic material, the elastic parts in equation (2.3) are given by

$$\kappa_t^e = \frac{1}{EI} M_t \tag{2.4a}$$

$$\gamma_t^e = K Q_t \tag{2.4b}$$

where

$K = k'A_bG$ where

k' = shear coefficient;

A_b = cross sectional area of the beam;

G = shear modulus;

$B = EI$ = flexural rigidity of the beam.

In order to determine the plastic deformations, a criterion is necessary to decide when plastic flow occurs in the beam. This is accomplished by specifying a yield surface in the moment–shear space. The choice of a yield surface in bending presents difficulties as we have to deal with stress resultants like moment and shear force rather than the stresses themselves. As Drucker [16] points out, it is not possible to determine the values of bending moment and shearing force which produce a condition of full plasticity at a particular cross section without considering the geometry and the loading of the entire beam. Thus, for a given cross section there does not exist a unique interaction curve in moment–shear space which corresponds to the locus of states at which plastic flow commences. Nevertheless, the introduction of an approximate moment–shear interaction curve is useful as long as we recognize that it is by no means unique or exact. To this end we assume that the initial yield surface is given by

$$\left(\frac{M}{M_0}\right)^{2n} + \left(\frac{Q}{Q_0}\right)^{2n} = 1 \tag{2.5}$$

where

M_0 = yield moment in simple bending = $\sigma_0 bh^2/6$;

Q_0 = yield shear force = $\frac{2}{3}\sigma_0 bh/\theta$;

σ_0 = yield stress in uniaxial tension;

b = width of the cross-section of the beam;

h = thickness of the beam;

$\theta = \begin{cases} \sqrt{3} \text{ for the von Mises criterion of yielding;} \\ 2 \text{ for the Tresca shear criterion;} \end{cases}$

$n = 1, 2, 3, \ldots$.

By assigning different values for n i.e. $n = 1, 2, 3, \ldots$, the shape of the initial yield surface can be changed and the effect of the yield surface on the solution can be studied. As plastic deformation takes place the stress resultants Q, M are assumed to lie on the loading surface given by

$$f(M, Q) = \left(\frac{M}{M_0}\right)^{2n} + \left(\frac{Q}{Q_0}\right)^{2n} - J^{2n} = 0 \tag{2.6}$$

where J is a yield parameter which depends on the extent of strain hardening. Subsequently, J will be assumed to be a function of the plastic work density W^p. The determination of $J(W^p)$ from results of a plastic bending test can be obtained from equation (2.13).

Although the shape of the yield surface has been selected in a rather arbitrary manner, later it will be shown that the numerical results are not very sensitive to the shape selected so that the nature of the yield function chosen is not critical.

We assume that the plastic strain rate vector is normal to the yield surface in the moment–shear space. This assumption, is analogous to that of requiring the material behavior to satisfy Drucker's stability postulate [17]; however, it does not follow directly

from this postulate due to the non-existence of a unique yield curve in the moment–shear space as discussed previously. Thus we have,

$$\kappa_t^p = \lambda \frac{\partial f}{\partial M} \tag{2.7a}$$

$$\gamma_t^p = \lambda \frac{\partial f}{\partial Q} \tag{2.7b}$$

where λ is a positive scalar function to be specified subsequently and $f(M, Q)$ is the yield function.

The derivation of the generalized stress–strain relations outlined here is very similar to that given by Clifton [18] in his analysis of combined torsional and longitudinal waves in a thin walled tube. We adopt a hardening law similar to the isotropic work-hardening model for the case of combined stresses in quasi-static plasticity. In the latter model, the plastic work density is used as the parameter relating the case of combined stresses to uniaxial stress–strain tests. In a similar manner we use the plastic work density to relate the case of bending under the combined influence of moment and shear force to the case of pure bending under the action of moment alone. There is little information available on hardening in bending and thus the choice of an "isotropic" hardening theory, although reasonable, is quite arbitrary. Its use can be justified only on basis of the agreement of the theoretical results to experimental data.

The plastic work rate is given by

$$W_t^p = M\kappa_t^p + Q\gamma_t^p. \tag{2.8}$$

Assuming that J in (2.6) is a monotonic function of W^p we can write

$$W_t^p = \frac{dW^p}{dJ} J_t. \tag{2.9}$$

Then from (2.6)–(2.9) we obtain

$$\lambda = \frac{dW^p}{dJ} \frac{J_t}{2nJ^{2n}}. \tag{2.10}$$

In analogy with the example for combined stresses [18] we use the case of pure bending to determine the function $W^p(J)$. If $M = M(\kappa)$ is the moment–curvature relation in pure bending, an increment in the moment dM is related to the increment in the elastic curvature $d\kappa^e$ and the increment in the plastic curvature $d\kappa^p$ by

$$dM = \frac{dM}{d\kappa}(d\kappa^e + d\kappa^p). \tag{2.11}$$

If the slope of the moment–curvature curve is expressed as a function of the moment i.e. $dM/d\kappa = g(M)$, we have

$$dM = g(M)\left\{\frac{dM}{B} + \frac{dW^p}{M}\right\} \tag{2.12}$$

since $d\kappa^e = dM/B$ and $dW^p = Md\kappa^p$ for pure bending. The yield condition reduces to $M = M_0J$ for pure bending and using this in (2.12) we have

$$\frac{dW^p}{dJ} = M_0^2 J \left\{\frac{1}{g(M_0J)} - \frac{1}{B}\right\}. \tag{2.13}$$

Using equations (2.13), (2.10), (2.7) and (2.4) in (2.3) we have

$$\kappa_t = \frac{M_t}{B} + \frac{1}{J^{4n-2}} \left\{ \frac{1}{g(M_0 J)} - \frac{1}{B} \right\} \left\{ \left(\frac{M}{M_0}\right)^{4n-2} M_t + \frac{M^{2n-1}Q^{2n-1}}{M_0^{2n-2}Q_0^{2n}} Q_t \right\} \qquad (2.14a)$$

$$\gamma_t = \frac{Q_t}{K} + \frac{1}{J^{4n-2}} \frac{M_0^2}{Q_0^2} \left\{ \frac{1}{g(M_0 J)} - \frac{1}{B} \right\} \left\{ \frac{M^{2n-1}Q^{2n-1}}{M_0^{2n}Q_0^{2n-2}} M_t + \left(\frac{Q}{Q_0}\right)^{4n-2} Q_t \right\}. \qquad (2.14b)$$

From (2.2) we have

$$\omega_x = \kappa_t$$
$$v_x - \omega = \gamma_t. \qquad (2.15)$$

Substituting (2.14) in (2.15) we have

$$N_1 M_t - \omega_x + HQM Q_t = 0$$
$$N_2 Q_t - v_x + \omega + HQM M_t = 0 \qquad (2.16)$$

where

$$H^* = \frac{1}{Q_0^{2n} M_0^{2n-2} J^{4n-2}} \left\{ \frac{1}{g(M_0 J)} - \frac{1}{B} \right\};$$

$$N_1 = \frac{1}{B} + H^* \left(\frac{Q_0}{M_0}\right)^{2n} M^{4n-2};$$

$$N_2 = \frac{1}{K} + H^* \left(\frac{M_0}{Q_0}\right)^{2n} Q^{4n-2};$$

$$H = H^* M^{2n-2} Q^{2n-2}.$$

When the loading is in the elastic range, H is equal to zero and the equations reduce to the familiar elastic equations. Equations (2.16) along with (2.1) constitute a system of four first order partial differential equations for the functions M, Q, ω and v. We seek a solution of these equations which satisfies the initial conditions

$$\omega(x, 0) = v(x, 0) = M(x, 0) = Q(x, 0) = 0 \qquad (2.17a)$$

and the boundary conditions (see Refs. [14, 15])

$$\omega(0, t) = 0$$
$$\frac{2Q(0, t)}{A} + \rho_r \hat{c} v(0, t) = -\rho_r \hat{c} V_0(t) \qquad (2.17b)$$

where

$$\hat{c} = \sqrt{\left(\frac{E_r}{\rho_r}\right)} = \text{velocity of propagation of longitudinal waves in the rod};$$

A = area of the rod;
E_r = Young's Modulus of the material of the rod;
ρ_r = mass density of the material of the rod.

The boundary condition (2.17b) makes use of the assumption that the wave propagation in the rod can be described by the elementary one dimensional theory for elastic rods.

3. CHARACTERISTIC PROPERTIES OF THE EQUATIONS

Equations (2.16) and (2.1) can be written in more compact form by introducing vector notation, as follows

$$L(\mathbf{w}) = A\mathbf{w}_t + B\mathbf{w}_x + C\mathbf{w} = 0 \tag{3.1}$$

where

$$\mathbf{w} = \begin{bmatrix} \omega \\ M \\ v \\ Q \end{bmatrix} \qquad A = \begin{bmatrix} \rho I & 0 & 0 & 0 \\ 0 & N_1 & 0 & HQM \\ 0 & 0 & \mu & 0 \\ 0 & HQM & 0 & N_2 \end{bmatrix}$$

$$B = \begin{bmatrix} 0 & -1 & 0 & 0 \\ -1 & 0 & 0 & 0 \\ 0 & 0 & 0 & -1 \\ 0 & 0 & -1 & 0 \end{bmatrix} \qquad C = \begin{bmatrix} 0 & 0 & 0 & -1 \\ 0 & 0 & 0 & 0 \\ 0 & 0 & 0 & 0 \\ +1 & 0 & 0 & 0 \end{bmatrix}.$$

Equation (3.1) constitutes a system of quasi-linear symmetric hyperbolic equations of first order. In the special case when the loading is elastic, the system becomes linear as N_1 and N_2 reduce to constants. The theory of quasi-linear symmetric hyperbolic equations is given in [19].

The characteristic velocities for (3.1) are the roots of the characteristic equation

$$\det(cA - B) = 0 \tag{3.2}$$

which can be written as

$$\rho I \mu N_3 c^4 - (\rho I N_1 + \mu N_2) c^2 + 1 = 0, \tag{3.3}$$

where

$$N_3 = N_1 N_2 - (HQM)^2.$$

The roots of (3.3) are

$$c^2 = \frac{(\rho I N_1 + \mu N_2) \pm \sqrt{[(\rho I N_1 + \mu N_2)^2 - 4\rho I \mu N_3]}}{2\rho I \mu N_3}. \tag{3.4}$$

The faster wave speed c_f is obtained by taking the $+$ sign and the slow wave speed c_s by taking the $-$ sign. For the elastic case, c_f corresponds to the velocity of propagation of longitudinal waves $c_1 = \sqrt{(B/\rho I)}$ while c_s corresponds to the velocity of propagation of shear waves $c_2 = \sqrt{(K/\mu)}$. The characteristic curves are the four families of curves in the t–x plane which satisfy

$$\frac{dx}{dt} = \pm c_f \quad \text{and} \quad \frac{dx}{dt} = \pm c_s. \tag{3.5}$$

For each characteristic velocity c there is a corresponding vector $\mathbf{l}$ which is a null vector of the characteristic matrix $\hat{C} = (cA - B)$ (i.e. $\mathbf{l}$ satisfies $\hat{C}\mathbf{l} = 0$). The four null vectors so

defined are linearly independent. The null vectors for the positive wave velocities are given, to within an arbitrary scalar multiplier, by

$$
l_f^+ = \begin{bmatrix} HQMc_f \\[6pt] -\rho I c_f^2 HQM \\[6pt] \dfrac{1}{\mu c_f} - \dfrac{\rho I c_f N_1}{\mu} \\[6pt] -1 + \rho I c_f^2 N_1 \end{bmatrix} \text{for} \quad \frac{\mathrm{d}x}{\mathrm{d}t} = +c_f \tag{3.6a}
$$

$$
l_s^+ = \begin{bmatrix} \dfrac{1}{\rho I c_s} - \dfrac{\mu c_s N_2}{\rho I} \\[6pt] \mu c_s^2 N_2 - 1 \\[6pt] HQMc_s \\[6pt] -\mu c_s^2 HQM \end{bmatrix} \text{for} \quad \frac{\mathrm{d}x}{\mathrm{d}t} = +c_s. \tag{3.6b}
$$

The null vectors l_f^- and l_s^- corresponding to characteristics $\mathrm{d}x/\mathrm{d}t = -c_f$ and $\mathrm{d}x/\mathrm{d}t = -c_s$ are obtained by substituting $-c_f$ for c_f and $-c_s$ for c_s in (3.6). A jump in the normal derivative of $\mathbf{w}$ across a characteristic curve is proportional to the corresponding null vector.

The interpretation of characteristic curves that is important from the point of view of numerical analysis is that along these curves, the partial differential equations reduce to ordinary differential equations. The ordinary differential equation associated with a characteristic for which the corresponding null vector is l is given by $l \cdot L(\mathbf{w}) = 0$ where the dot denotes the Euclidean inner product. Substituting (3.6) in the above equation we obtain

$$
(\mathrm{d}M - \rho I c_f \mathrm{d}\omega) + \alpha(\mathrm{d}Q - \mu c_f \mathrm{d}v) + (Qc_f + \mu c_f^2 \omega \alpha)\mathrm{d}t = 0 \quad \text{for} \frac{\mathrm{d}x}{\mathrm{d}t} = +c_f \tag{3.7a}
$$

$$
\beta(\mathrm{d}M - \rho I c_s \mathrm{d}\omega) + (\mathrm{d}Q - \mu c_s \mathrm{d}v) + (\mu c_s^2 \omega + Qc_s \beta)\mathrm{d}t = 0 \quad \text{for} \frac{\mathrm{d}x}{\mathrm{d}t} = +c_s \tag{3.7b}
$$

where

$$
\alpha = \frac{\dfrac{1}{\mu c_f^2} - \dfrac{\rho I N_1}{\mu}}{HQM} = \frac{HQM}{\dfrac{1}{\rho I c_f^2} - \dfrac{\mu N_2}{\rho I}} = \frac{-\rho I}{\mu}\beta \tag{3.8}
$$

and

$$
\beta = \frac{\dfrac{1}{\rho I c_s^2} - \dfrac{\mu N_2}{\rho I}}{HQM} = \frac{HQM}{\dfrac{1}{\mu c_s^2} - \dfrac{\rho I N_1}{\mu}} = \frac{-\mu}{\rho I}\alpha. \tag{3.9}
$$

The incremental relations along the characteristics $dx/dt = -c_f$ and $dx/dt = -c_s$ are obtained by replacing c_f and c_s by $-c_f$ and $-c_s$, respectively, in (3.7). For the familiar example of elastic loading of the beam, the characteristic relations (3.7) reduce to

$$dM - \rho I c_1 \, d\omega + Q c_1 \, dt = 0; \qquad \frac{dx}{dt} = +c_1$$

$$dQ - \mu c_2 \, dv + \mu c_2^2 \omega \, dt = 0; \qquad \frac{dx}{dt} = +c_2. \tag{3.10}$$

The coefficients α and β in the incremental relations (3.7) need special consideration for stress states on the moment axis and on the shear axis. The cases $M = 0$ and $Q = 0$ are considered separately.

Case (a): $M = 0$

In this case the expressions for the wave speeds reduce to

$$c_f = c_1$$

$$c_s = \sqrt{\left(\frac{1}{\mu N_2}\right)}.$$

From the second expression for α in (3.8) it follows that both α and β are zero. Thus, the incremental relations reduce to

$$(dM - \rho I c_f \, d\omega) + Q c_f \, dt = 0 \quad \text{for } \frac{dx}{dt} = c_f \tag{3.11a}$$

$$(dQ - \mu c_s \, dv) + \mu c_s^2 \omega \, dt = 0 \quad \text{for } \frac{dx}{dt} = c_s. \tag{3.11b}$$

Case (b): $Q = 0$

In this case we consider separately the intervals $M_0 < |M| < \hat{M}$ and $|M| > \hat{M}$, where $\hat{M}$ is the moment for which the wave speeds c_f and c_s are equal. The moment $\hat{M}$ corresponds to the point on the moment–curvature curve where the slope is equal to $\rho I K/\mu$.

For the interval $M_0 < |M| < \hat{M}$ the expressions for the wave speeds reduce to

$$c_f = \sqrt{\left(\frac{1}{\rho I N_1}\right)}$$

$$c_s = c_2.$$

In this interval it can be seen from the second expression for α that both α and β are zero so that the incremental relations are still given by (3.11).

For $|M| > \hat{M}$, the wave speeds are given by

$$c_f = c_2$$

$$c_s = \sqrt{\left(\frac{1}{\rho I N_1}\right)}.$$

From the first expression for α in (3.8) it is seen that α and β become infinite for this case. To avoid this difficulty we rewrite the incremental relations as follows

$$\alpha^*(dM - \rho Ic_f \, d\omega) + (dQ - \mu c_f \, dv) + (Qc_f\alpha^* + \mu c_f^2\omega) \, dt = 0 \quad \text{for } \frac{dx}{dt} = +c_f \qquad (3.12a)$$

and

$$(dM - \rho Ic_s \, d\omega) + \beta^*(dQ - \mu c_s \, dv) + (\mu c_s^2\omega\beta^* + Qc_s) \, dt = 0 \quad \text{for } \frac{dx}{dt} = +c_s \qquad (3.12b)$$

where

$$\alpha^* = \frac{HQM}{\dfrac{1}{\mu c_f^2} - \dfrac{\rho IN_1}{\mu}} \quad \text{and} \quad \beta^* = -\frac{\rho I}{\mu}\alpha^*. \qquad (3.13)$$

From (3.13) it follows that for $Q = 0$ and $|M| > \hat{M}$ the coefficients α^* and β^* reduce to zero. Then the incremental relations simplify to

$$(dQ - \mu c_f \, dv) + \mu c_f^2\omega \, dt = 0 \quad \text{for } \frac{dx}{dt} = +c_f \qquad (3.14a)$$

$$(dM - \rho Ic_s \, d\omega) + Qc_s \, dt = 0 \quad \text{for } \frac{dx}{dt} = +c_s. \qquad (3.14b)$$

In order to facilitate numerical computations the moment–shear space is divided into two regions (see Fig. 4). In region I the incremental relations given in (3.7) are used whereas in region II the incremental relations given in (3.12) are used. In this way the coefficients used in the computations always remain bounded.

4. NUMERICAL SCHEME

The difference method adopted here is a second order accurate extension of the method proposed by Courant *et al.* [20]. The method is second order accurate in that if the solution were known at some time, the error introduced during the next time step Δt would be $0(\Delta t^3)$. Proof of convergence of the method as well as a discussion of its computational advantages relative to other second order accurate methods has been given by the authors [21].

The mesh points chosen for numerical integration of the incremental relations (3.7) are the intersections of the lines $x = (K-1)\Delta x$ and $t = (I-1)\Delta t$ for $K = 1, 2, \ldots$ and $I = 1, 2 \ldots$ where Δx and Δt are the increments in x and t, respectively. Let the discrete functions $\hat{\omega}$, $\hat{M}$, $\hat{Q}$, $\hat{v}$ and $\hat{J}$ correspond to the functions ω, M, Q, v and J respectively, at the grid points. We have two kinds of grid points to consider—boundary points which are grid points on the line $x = 0$ in the x–t plane; interior points which correspond to the other points. The difference method presented here enables us to compute the solution at a mesh point on the line $t = t_0 + \Delta t$ knowing the solution **w** on the line $t = t_0$. At an interior point we integrate along the four characteristics through the new mesh point on the line $t = t_0 + \Delta t$ to obtain the solution at this point. At a boundary point, we integrate along

the two backward characteristics with negative slope and use the two boundary conditions to evaluate the solution at the new mesh point on the line $t = t_0 + \Delta t$.

Consider the calculation of the solution at a point P on the x–t plane from data known at mesh points Q_-, Q and Q_+ (Fig. 2). The four backward characteristics intersect the line $t = (I-1)\Delta t$ at points Q_1, Q_2, Q_3 and Q_4. The ratio $\Delta t/\Delta x$ is chosen equal to $1/c_1$ where $c_1 = \sqrt{(B/\rho I)}$. Since $c_f \leq c_1$, all the points Q_i, $i = 1, 2, 3, 4$ lie between Q_- and Q_+. Thus the point P lies within the domain of influence of the line Q_-Q_+. This satisfies the requirement of convergence and stability outlined in [22].

We integrate the incremental relations along the characteristics from the point P to the intersection with the line $t = (I-1)\Delta t$. The incremental relation along the ith characteristic is of the form

$$\sum_{j=1}^{4} \alpha_{ij}(\mathrm{d}w_j)_i + \beta_i \,\mathrm{d}t = 0 \qquad i = 1, 2, 3, 4 \tag{4.1}$$

where $(\mathrm{d}w_j)_i$ is the increment in the jth component of the solution vectors along the ith characteristic. The coefficients α_{ij} are constants for the elastic case; but for the plastic case they are dependent on the vector $\mathbf{w}$. The term β_i is dependent on the solution vector in both the cases. For the elastic case, integration of (4.1) yields

$$\sum_{j=1}^{4} \alpha_{ij}[\hat{w}_j(P) - \hat{w}_j(Q_i)] + \{\beta_i(P) + \beta_i(Q_i)\}\frac{\Delta t}{2} = 0 \tag{4.2}$$

where

$$\hat{w}_j(Q_i) = \hat{w}_j(Q) + \lambda_i\left(\frac{\hat{w}_j(Q_+) - \hat{w}_j(Q_-)}{2}\right) + \frac{\lambda_i^2}{2}\{\hat{w}_j(Q_+) - 2\hat{w}_j(Q) + \hat{w}_j(Q_-)\}$$

where

$$Q_i = Q + \left(\frac{Q_+ - Q_-}{2}\right)\lambda_i.$$

For the plastic case we use a two step integration routine. In the first step, we assume the coefficients to be constant and solve for $\mathbf{w}$. This solution is then refined in the next step. The intermediate solution $\mathbf{w}'$ is given by the equation

$$\sum_{j=1}^{4} \alpha_{ij}(Q)\{w'_j(P) - \hat{w}_j(Q_i)\} + \beta_i(Q_i)\Delta t = 0. \tag{4.3}$$

We use the intermediate solution to evaluate the average value of the coefficients α_{ij} and β_i denoted here by $\bar{\alpha}_{ij}$ and $\bar{\beta}_i$

$$\bar{\alpha}_{ij} = \tfrac{1}{2}\{\alpha_{ij}(P, \mathbf{w}'(P)) + \alpha_{ij}(Q_i, \hat{\mathbf{w}}(Q_i))\}$$

$$\bar{\beta}_i = \tfrac{1}{2}\{\beta_i(P, \mathbf{w}'(P)) + \beta_i(Q_i, \hat{\mathbf{w}}(Q_i))\}.$$

The final solution is then given by the equation

$$\sum_{j=1}^{4} \bar{\alpha}_{ij}\Delta\hat{w}_j = \sum_{j=1}^{4} \bar{\alpha}_{ij}\left\{\lambda_i\left(\frac{\hat{w}(Q_+) - \hat{w}(Q_-)}{2}\right) + \frac{\lambda_i^2}{2}(\hat{w}(Q_+) - 2\hat{w}(Q) + \hat{w}(Q_-))\right\} - \bar{\beta}_i\Delta t \tag{4.4}$$

where

$$\Delta\hat{w}_j = \hat{w}_j(P) - \hat{w}_j(Q). \tag{4.5}$$

Equations (4.4) constitute a set of 4 equations involving data at mesh points Q_+, Q and Q_- and they can be solved to give the increment in the solution $\Delta\hat{w}$ and hence the solution at an interior point P. At a boundary point, 2 equations similar to (4.4) together with the two boundary conditions (2.15) yield the final solution.

In wave propagation problems of this type, loading and unloading takes place along the beam. Thus both elastic and plastic regions occur so that it is necessary at each point to decide whether the equations for elastic or plastic regions are to be used. The procedure adopted for this choice is as follows:

1. After each calculation, the function $J = [(M/M_0)^{2n} + (Q/Q_0)^{2n}]^{1/2n}$ is calculated. If $J > J_{max}$ then J_{max} is updated to the value J. J_{max} is initially set equal to unity.

Before computing the solution at a new point P, the function J at the point Q is calculated. If $J(Q) < J_{max}(Q)$ then equations for elastic regions are used. If $J(Q) = J_{max}(Q)$, then equations for plastic regions are used.

2. If the new value of J at P confirms the choice made in (1), we move to the next point. If not, the alternative choice is taken and a new evaluation of the solution at P is made. If this satisfies the second choice we proceed to the next point.

3. If neither choice is satisfactory, then the cells adjacent to such points are subdivided into sixteen cells each. Second order accurate interpolation is used to compute the solution at the new mesh points at time $t = t_0$. With the smaller mesh size, we follow the same scheme as explained in (1) and (2) except that we do not check for the second alternative as before. This procedure of reducing the mesh size was introduced because experience showed that various averaging procedures used for such points led to large errors in the computed solution. With the reduced mesh size the magnitude of the errors introduced is greatly reduced.

Special attention must be given to the computation of the numerical solution at mesh points where the stress state is near $Q = 0$, $M = \hat{M}$ in the moment–shear space. At such points it is possible that the coefficient $\bar{\alpha}_{ij}$ in equation (4.4) would be obtained by averaging the value of α_{ij} corresponding to points in regions I and II (Fig. 4). This would lead to an incorrect solution since the coefficients are defined differently in these two regions. This difficulty was avoided by computing the solution at such transitional points by means of the first order accurate system of equations, equations (4.3), in which the coefficients are all evaluated at one point. Since such cases arise at only a few points, the numerical results are still, essentially second order accurate.

A measure of the error between the numerical solution and the actual solution of the differential equations is useful in judging the accuracy of the numerical results. Such a measure is obtained by checking the energy balance in the system, i.e. the work input to the system must equal the sum of the plastic work done and the increase in the kinetic energy and the elastic strain energy of the system. The actual solution $\mathbf{w}$ satisfies the equation

$$\iint \mathbf{w} \cdot L(\mathbf{w}) \, dx \, dt = 0 \tag{4.6}$$

where $L(w)$ is the operator defined in (3.1). Equation (4.6) can be reduced to

$$\int \frac{1}{2}\left(\rho I \omega^2 + \mu v^2 + \frac{M^2}{B} + \frac{Q^2}{K}\right) dx + \iint M_0^2 \left(\frac{1}{g(M_0 J)} - \frac{1}{B}\right) J \, dJ \, dx = \int -\{(M\omega + Qv)|_{x=0}\} \, dt. \tag{4.7}$$

Equation (4.7) is recognized as a statement of energy balance of the system. The first term on the left hand side represents the sum of the kinetic energy and the elastic strain energy of the system while the second term represents the total plastic work done. The term on the right hand side represents the work supplied to the system. We now define the "error" in numerical computation as follows:

$$\text{Error} = \frac{\text{"total" energy} - \text{work input}}{\text{work input}} \tag{4.8}$$

where "total" energy and work input are, respectively, the left and right hand sides of (4.7).

5. EXPERIMENTAL PROCEDURE

The experimental set-up is described in detail in [15] (see Fig. 1). The striker bar on impact with the loading bar transmits an approximately rectangular pulse of $100 \, \mu\text{sec}$ duration, through the loading bar. The pulse is reflected at the interface between the loading bar and the beam. The loading bar and the beam are sufficiently long so that no wave reflections occurred during the first $100 \, \mu\text{sec}$ after impact. The loading bar ($\frac{3}{8}$ in. diameter) is made of hardened steel with a yield stress of over $100,000 \, \text{psi}$ so that the strains in the rod remain in the elastic range. The ends of the loading bar were rounded slightly so that the load was transmitted to the beam on a smaller area. The incident stress pulse in the rod had a rise time of approximately $10 \, \mu\text{sec}$. This was accounted for, in the theoretical solution, by considering a parabolic rise in the function $V(t)$ with the full velocity V_0 being reached after $10 \, \mu\text{sec}$.

The material of the beams used in the experiments was chosen to be an aluminum alloy in order to minimize the effects of strain-rate sensitivity. The particular alloy chosen (6063) was selected because of its availability in convenient sizes and its low yield strength. The use of a soft material enables us to use moderate impact velocities and still obtain plastic strains which are large relative to the yield point strain so that the plastic flow characteristics of the material are of primary importance in determining the response of the beam.

The 6063 alloy of aluminum has the following nominal chemical composition [23]:

TABLE 1

Silicon (%)	Magnesium (%)	Aluminum (%)
0·4	0·7	98·9

The bar stock in the T5 state has a tabulated tensile yield strength of $21,000 \, \text{psi}$ [23]. The specimen used was $\frac{3}{16}$ in. thick, $\frac{1}{2}$ in. wide and 38 in. long. It was annealed to reduce it to a state of zero temper with a yield strength of $3000 \, \text{psi}$. In the annealing process, the temperature is raised to $750°\text{F}$ in approximately 6 hr and held at that temperature for 2 hr. The specimens are then brought down to a temperature of $500°\text{F}$ at the rate of $50°\text{F/hr}$ and finally left to cool in the oven. For each beam specimen tested dynamically, two short specimens cut from the region of stock material adjacent to the ends of the beam specimen were used for quasi-static stress–strain tests. These short specimens are 8 in. long and go

through the same annealing as the long beam specimens. Quasi-static stress–strain tests were conducted on these annealed sample specimens using an Instron Universal testing machine. From this stress–strain curve, the corresponding moment–curvature relation is obtained as follows.

$$M = 2 \int_0^{h/2} \sigma bz \, dz \tag{5.1}$$

where
$h =$ thickness of the beam;
$b =$ width of the beam.
Writing $z = \varepsilon/\kappa$ where ε is the strain in a fiber at a distance z from the neutral axis and κ is the curvature we have

$$M = \frac{2b}{\kappa^2} \int_0^{\kappa h/2} \sigma(\varepsilon)\varepsilon \, d\varepsilon \tag{5.2}$$

where $\sigma = \sigma(\varepsilon)$, a function of the strain.
If ε_0 is the yield strain (5.2) becomes

$$M = \frac{2b}{\kappa^2}\left[\frac{E\varepsilon_0^3}{3} + \int_{\varepsilon_0}^{\kappa h/2} \sigma(\varepsilon)\varepsilon \, d\varepsilon\right] \quad \text{for } \kappa > \frac{2\varepsilon_0}{h}$$

$$M = EI\kappa \quad \text{for } \kappa \leq \frac{2\varepsilon_0}{h} \tag{5.3}$$

knowing $\sigma = \sigma(\varepsilon)$ from the stress–strain data, the moment corresponding to a specific value of the curvature can be obtained. Simpson's rule was used to evaluate the integrals in (5.3). For the numerical calculations presented here, an empirical moment–curvature relation was obtained to fit the experimental values.

$$(\kappa - \kappa_0) = \frac{(M - M_0)}{EI} + D(M - M_0)^C \tag{5.4}$$

where
$M =$ bending moment; $M_0 =$ yield moment;
$\kappa =$ curvature; $\kappa_0 =$ yield curvature.
D and C are constants obtained by using the method of least squares to minimize the difference between the experimental values and the empirical fit. Figure 3 shows a comparison of the moment–curvature curves obtained from experimental results and the empirical relation. It is seen that the empirical relation fits the experimental curve fairly well. Stress–strain tests were conducted on each batch of specimens and an empirical fit was obtained for beam specimens belonging to that batch. Typical values for the constants in (5.4) for one batch of specimens are given here:

$E = 10 \cdot 2 \times 10^6$ psi;
$I = 0 \cdot 276 \times 10^{-3}$ in.^{4};
$M_0 = 7 \cdot 81$ lb in.;
$\kappa_0 = 0 \cdot 276 \times 10^{-2}$ in.$^{-1}$;
$D = 0 \cdot 267 \times 10^{-4}$;
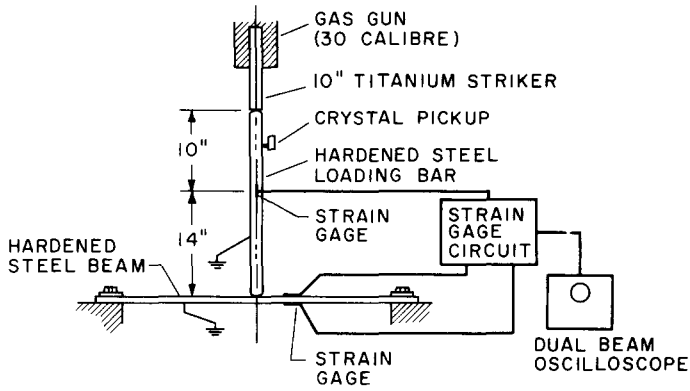$C = 2 \cdot 84.$

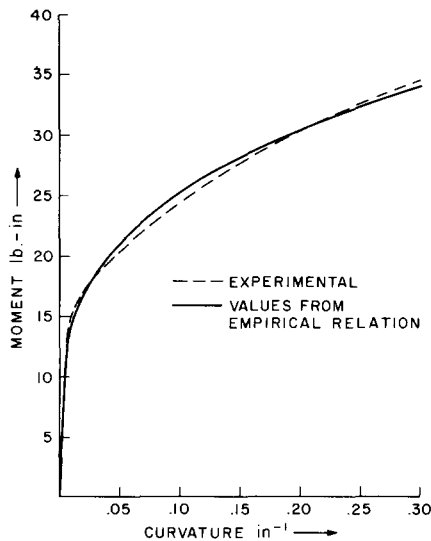FIG. 1. Experimental set up.
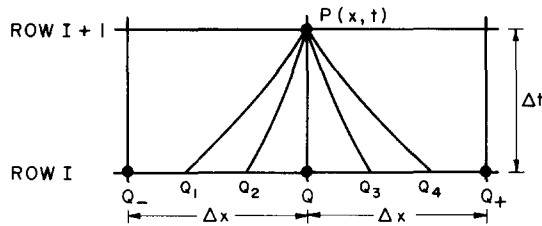
FIG. 2. Grid and characteristics.

FIG. 3. Comparison of experimental and empirical moment–curvature relations.

$$\left(\frac{M}{M_0}\right)^{2n} + \left(\frac{Q}{Q_0}\right)^{2n} = 1$$

REGION I

REGION II

$\frac{\hat{M}}{M_0}$
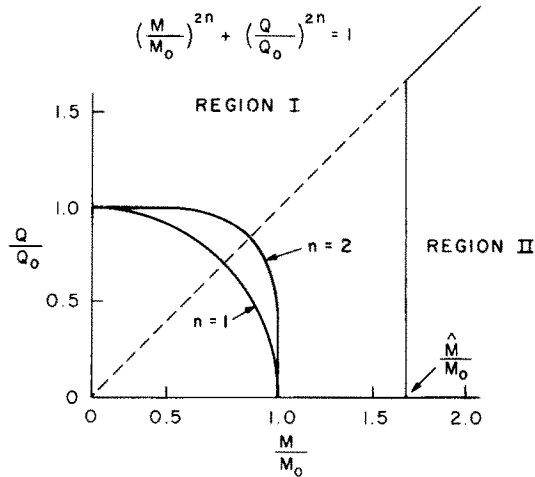
$\frac{Q}{Q_0}$

$\frac{M}{M_0}$

n = 2

n = 1

FIG. 4. Yield surface in the moment–shear space.

The yield moment M_0 was taken to be that value of the moment where the first deviation from linearity was observed in the quasi-static curve. Foil strain gages (BLH type FAE-12-12S13L and FAE-12-12PL) with $\frac{1}{8}$ in. gage length were used to record the strain in the beam. The latter variety is of the post yield type but both gages can take strains up to 5 per cent without loss of linearity. The post yield gages were used at points closer to the point of impact where there was substantial yielding. The strain gages were bonded to the beam using EPY 150 cement and the bond was cured for 24 hr before the gages were used. A similar gage of $\frac{1}{8}$ in. gage length was used to record the strain in the rod. A constant current strain gage circuit is used to make dynamic strain measurements in the beam. The strain output was calibrated by switching a known resistance in parallel with the strain gage to produce an apparent strain and the manufacturer's gage factor was used to convert the observed change in voltage to an equivalent strain. The strain profiles were displayed on a Tektronix 556 dual beam oscilloscope and pictures of the traces were taken using Polaroid type 46 film. The oscilloscopes were triggered using a piezoelectric crystal phonograph cartridge which was mounted on the loading bar. The needle of the cartridge rests lightly on the loading bar and is excited laterally when a stress pulse passes it. The output of the crystal is sufficient to trigger the oscilloscopes without difficulty. Figures 5(a)–(f) show a few pictures of the oscilloscope traces at different positions along the length of the beam for different velocities of impact.

In the first series of tests the strain response was obtained at distances $x = \frac{1}{2}, 1, 1\frac{1}{2}, 2$ and $2\frac{1}{2}$ in. from the point of impact on the beam. Measurements were also made of the incident and reflected waves in the rod. The strain responses at different positions along the beam in general correspond to different velocities of impact as separate experiments were done for each case.

In the second series of tests, the strain–time profiles were obtained at one position $x = 1\frac{1}{2}$ in. for different velocities of impact. This enables a comparison with theoretical results for higher impact velocities where plastic strains predominate.

As a check on the assumption that the middle surface of the beam is unstrained, strain–time profiles for the upper and lower surfaces were compared. Typical results are shown
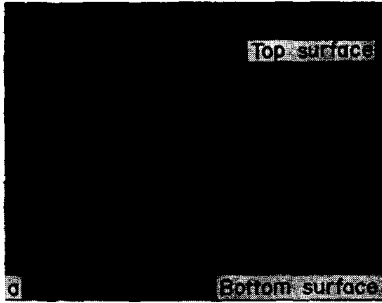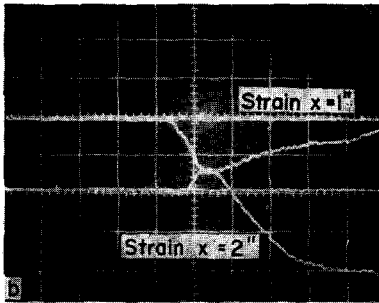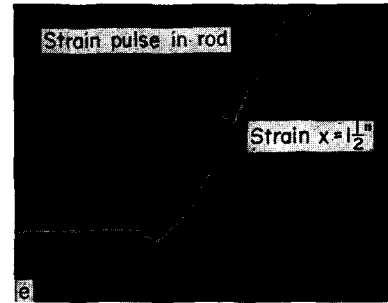
Comparison of surface strains at the top
and bottom surfaces
Strain calibration: Top surface 0·076%/cm
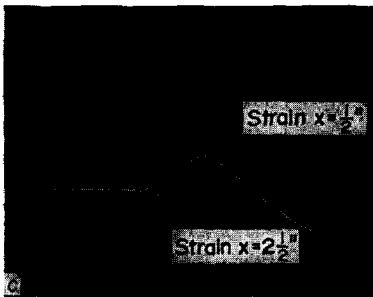Bottom surface 0·055%/cm
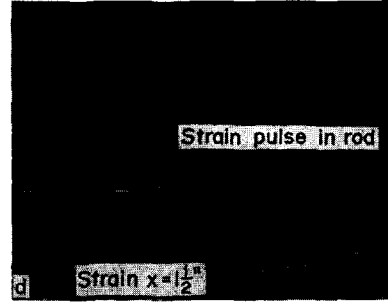
V_o = 333″/sec
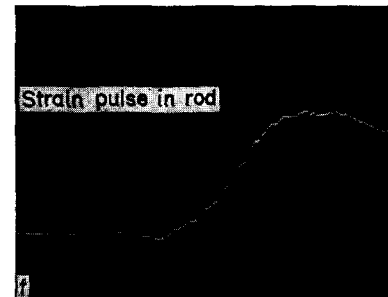Strain calibration: Beam x = $1\frac{1}{2}''$ 0·071%/cm
Rod 0·0295%/cm

V_o =240″/sec
Strain calibration: x = 1″ 0·076%/cm
x = 2″ 0·049%/cm

V_o =500″/sec
Strain calibration: Beam x = $1\frac{1}{2}''$ 0·072%/cm
Rod 0·042%/cm

V_o =340″/sec
Strain calibration: x = $\frac{1}{2}''$ 0·044%/cm
x = $2\frac{1}{2}''$ 0·044%/cm

V_o = 600″/sec
Strain calibration: Beam x = $1\frac{1}{2}''$ 0·158%cm
Rod 0·0425%/cm

FIG. 5. Strain–time profiles.

in Fig. 6. Since the strains at the two surfaces are essentially equal in magnitude but opposite in sign, the middle surface strain is small—say less than 2 per cent of the surface strain—and can safely be neglected.
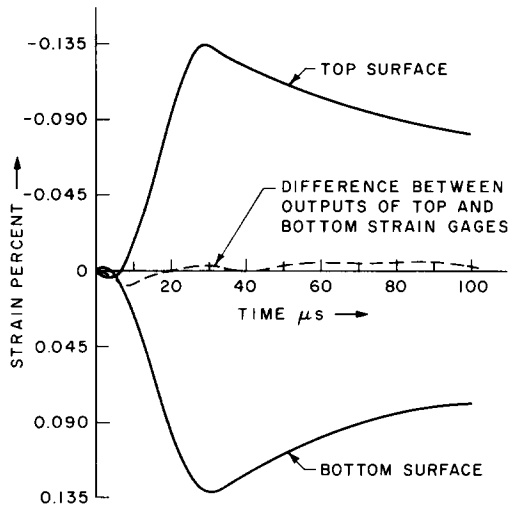
FIG. 6. Comparison of surface strains at the top and the bottom surfaces.

6. COMPARISON OF THEORY WITH EXPERIMENT

Numerical solutions of equation (3.1) have been obtained for impact velocities corresponding to those used in the experiments. For these calculations, the exponent n in the equation of the yield surface [equation (2.5)] was taken to be unity; comparisons of these results with the case $n = 2$ indicate that the solutions are relatively insensitive to the value of n. The effect of changing n is discussed in more detail later in this section. The solutions yield directly the values of M, ω, Q and v at mesh points. The surface strain in the beam has been obtained by integrating equation (2.14a) for the curvature rate and using the relation $\varepsilon = \kappa h/2$. The transverse velocity has been integrated with respect to time to give the transverse displacement.

For all the numerical solutions presented here, the mesh size has been taken sufficiently small for the "error" in the energy balance to be kept less than 2 per cent throughout the calculations. The mesh size used was $\Delta x = 0.05$ in. and $\Delta t = 0.25$ μsec.

The experimental and theoretical strain–time profiles are compared in Figs. 7–11. The theoretical predictions appear to be in reasonable agreement with experimental results with the agreement improving with distance from the point of impact. The closer agreement at more distant stations is similar to that observed in the study of elastic bending waves reported in [15]. The large discrepancy between theory and experiment shown in Fig. 7 is believed to be due in part to the slope of the empirical moment–curvature curve being a poor approximation to that of the actual moment–curvature curve for curvatures in the neighborhood of yield. This explanation is based on the observations that (i) the experimental strain–time profile in Fig. 7 lies between that computed from the empirical moment–curvature relation and that computed assuming elastic behavior (cf. Fig. 14)
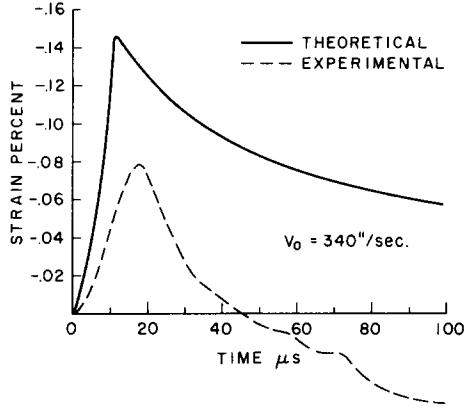
FIG. 7. Comparison of theoretical and experimental strain–time profiles at $x = \frac{1}{2}$ in.
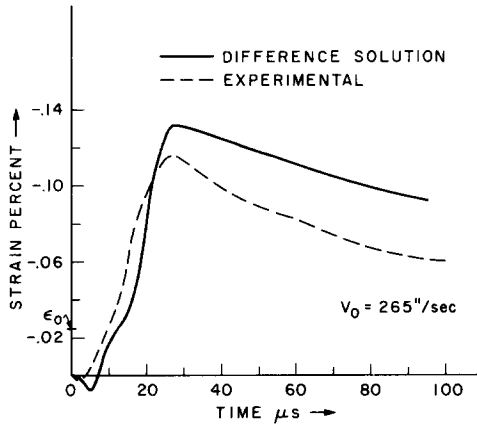
FIG. 8. Comparison of theoretical and experimental strain–time profiles at $x = 1$ in.
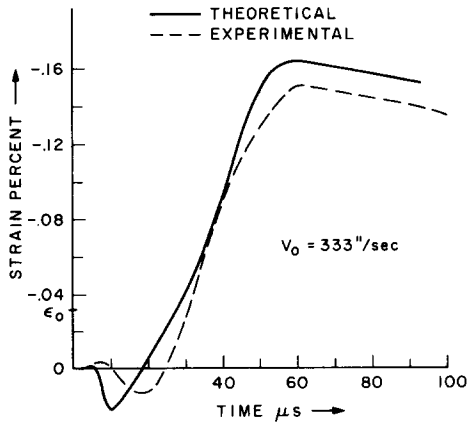
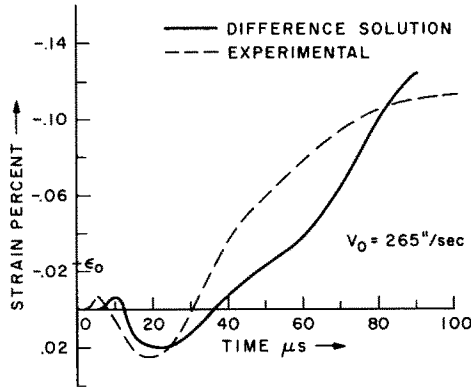FIG. 9. Comparison of theoretical and experimental strain–time profiles at $x = 1\frac{1}{2}$ in.

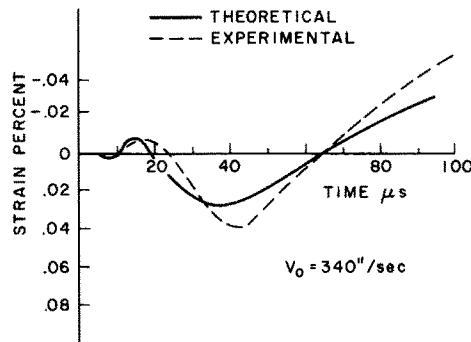FIG. 10. Comparison of theoretical and experimental strain–time profiles at $x = 2$ in.

FIG. 11. Comparison of theoretical and experimental strain–time profiles at $x = 2\frac{1}{2}$ in.

and (ii) the slope of the quasi-static moment–curvature curve lies between that of the empirical curve and the slope EI associated with the elastic response. Calculations for $V_0 = 333$ in./sec. (Fig. 9) for which the empirical moment–curvature curve was made to fit the experimental curve closely for small curvatures resulted in a strain–time profile for $x = \frac{1}{2}$ in. that was considerably closer to that observed in experiments than is the theoretical curve shown in Fig. 7 (e.g. $\varepsilon = -0.03$ per cent at $t = 60$ μsec.). However, there is no change in sign even at later times; and it does not appear that adjusting the empirical relation can lead to a change in sign at a time of approximately 50 μsec as observed in the experiments.

Figure 12 shows a comparison of the theoretical and experimental strain–time profiles at $x = 1\frac{1}{2}$ in. for three different impact velocities. These results correspond to the same batch of specimens with the same empirical moment–curvature relation. At higher impact velocities, the theory predicts a lower peak strain than is observed in the experiments. No satisfactory explanation has been found for this discrepancy.

The effect of increasing the strain rate in most metals is to increase the yield stress and raise the level of the stress–strain curve from that of the quasi-static stress–strain curve. In order to investigate the effect of higher strain rates, numerical solutions were obtained for the case where the yield moment M_0 and the yield curvature κ_0 in equation (5.4) was increased by 50 per cent. This raises the moment–curvature curve and thereby introduces an effect
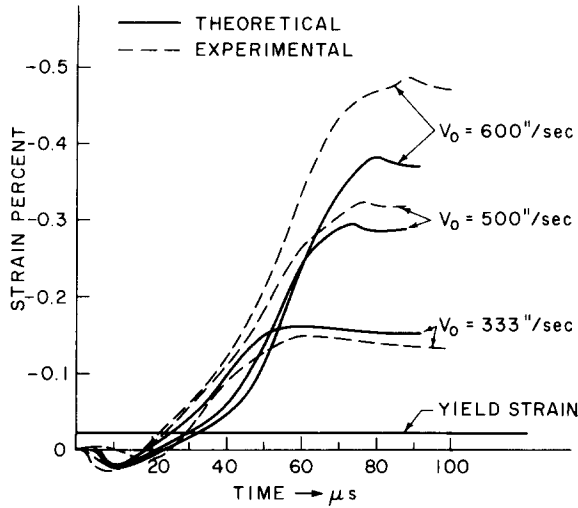
FIG. 12. Comparison of theoretical and experimental strain–time profiles at $x = 1\frac{1}{2}$ in. for different velocities.

which is similar to that due to high strain rates. Figures 13–17 compare the computed strain–time profiles corresponding to the raised moment–curvature curve with those calculated using the original quasi-static moment–curvature relation. In general the effect of increasing the yield moment was to improve the agreement between theory and experiment—especially at $x = \frac{1}{2}$ in. and $x = 1$ in. However, for the aluminum alloy used as the beam, strain rate effects are unlikely to cause an increase in the yield moment by anywhere near 50 per cent and even with such an increase, there is only a slight improvement in the agreement between theory and experiment. A more thorough study of the importance of strain rate sensitivity could be obtained by comparing the results of the present theory with the results from a theory based on a viscoplastic model, such as the one used by Bejda [24]. Figures 14–17 also show the theoretical and experimental strain profiles for
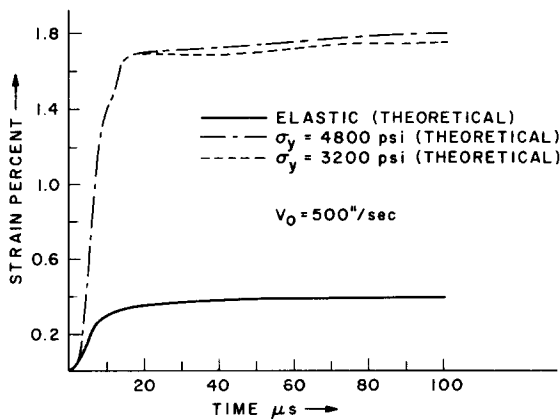

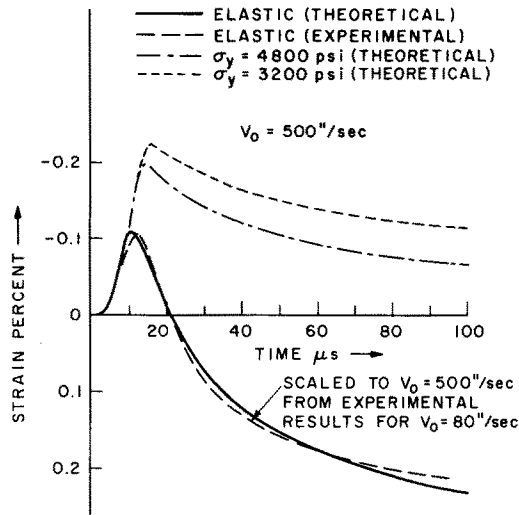FIG. 13. Effect of yield stress on predicted strain–time profile at $x = 0$ in.

FIG. 14. Effect of yield stress on predicted strain–time profile at $x = \frac{1}{2}$ in.

the beam, if the beam were completely elastic. The experimental strain response for the elastic case shown in Figs. 14–17 was scaled to $V_0 = 500$ in./sec from measurements for $V_0 = 80$ in./sec.

The numerical solution was computed for two different shapes of the yield surface (see Fig. 4) corresponding to values $n = 1$ and $n = 2$ in equation (2.5). Figure 18 shows a comparison of the predicted strain response at different positions along the beam for the two different yield surfaces. This example corresponded to a velocity of impact $V_0 = 500$ in./sec.
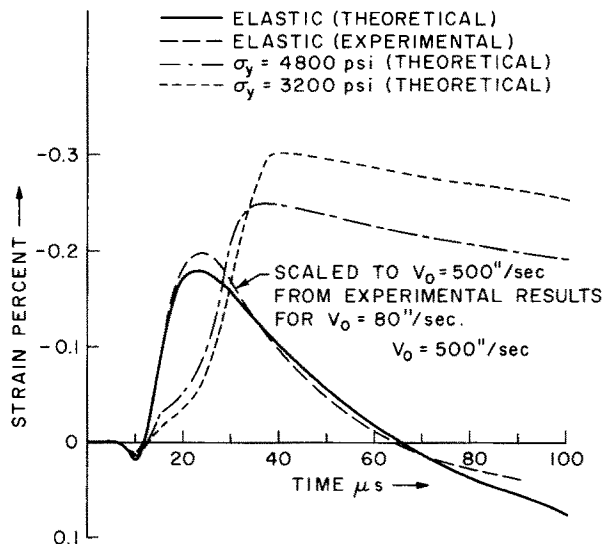

FIG. 15. Effect of yield stress on predicted strain–time profile at $x = 1$ in.
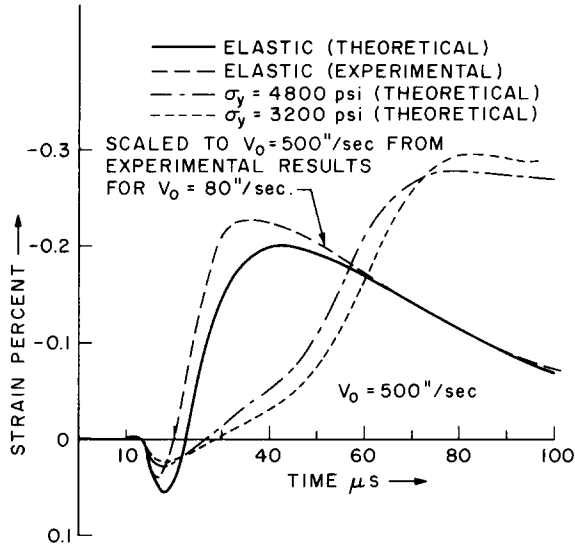
FIG. 16. Effect of yield stress on predicted strain–time profile at $x = 1\frac{1}{2}$ in.

The comparison shows that the predicted strain response is not very sensitive to the shape of the yield surface. The greatest discrepancy is at $x = 0$ where beam theory itself is of questionable validity; at distances where beam theory is expected to be a good approximation the discrepancies are completely negligible. Thus, the shape of the yield surface does not appear to be critical in predicting the dynamic response of the beam.
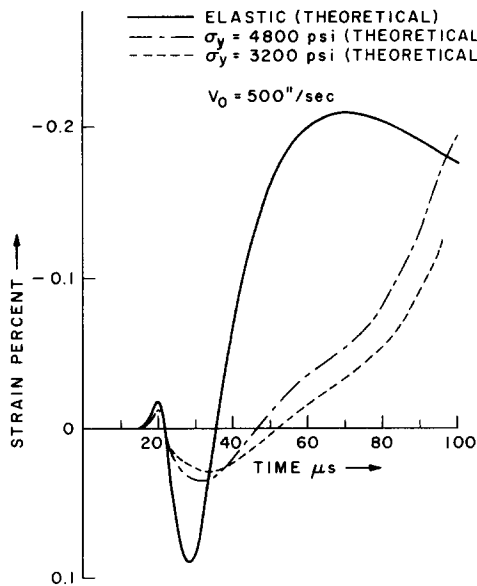

FIG. 17. Effect of yield stress on predicted strain–time profile at $x = 2$ in.
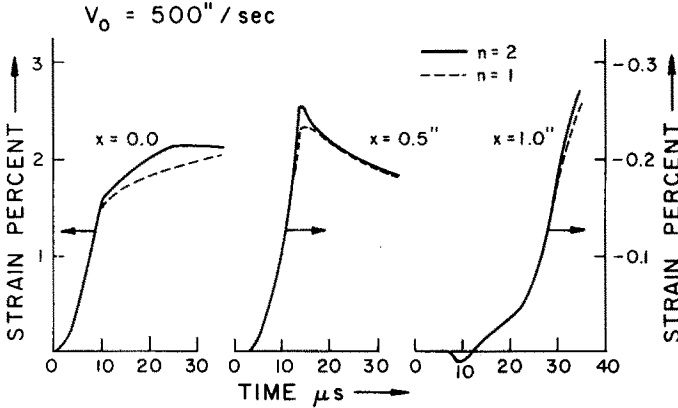
FIG. 18. Comparison of the predicted strain response for different shapes of yield surface.

Figure 19 shows the elastic–plastic boundaries in the x–t plane for $V_0 = 500$ in./sec. There are three distinct plastic regions, the central region corresponding to negative curvature rate whereas the other two regions correspond to positive curvature rate. For the range of time considered, the plastic deformation in region III is negligible relative to that in the other two regions. The resulting deformation is similar to that corresponding to a stationary plastic hinge with positive curvature rate at $x = 0$ and a travelling hinge with negative curvature rate as predicted by Conroy's solution [12] of the problem of constant velocity impact of an infinite, rigid, perfectly-plastic beam. Although the present
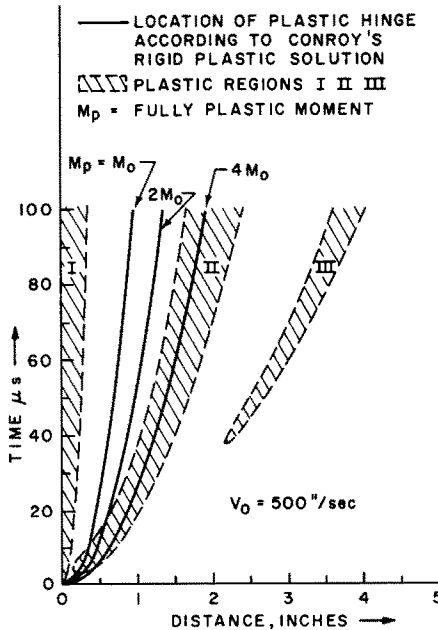

FIG. 19. Elastic–plastic boundaries.

problem differs from that considered by Conroy in several respects, a comparison of the present solution with that of Conroy is helpful for giving a physical interpretation to the numerical solutions obtained by means of the theory used here. To this end, the location of the travelling hinge according to Conroy's solution is shown in Fig. 19 for three different values of the fully plastic moment M_p. For $M_p = 4M_0$ the trajectory of the travelling hinge according to Conroy's solution agrees closely with the center line of region II. Since the present theory includes work hardening whereas Conroy's solution is for a perfectly plastic material, an appropriate value for M_p in Conroy's solution would be expected to be greater than M_0; however, no intrinsic importance should be attributed to this particular value of M_p which gives good agreement. Again, the purpose of the comparison in Fig. 19 is to illustrate that region II corresponds to a region with negative rate of curvature.

Region I in Fig. 19 corresponds to the stationary shear hinge and bending hinge of the solution by Karunes and Onat [25] of the problem of constant velocity impact of a rigid, perfectly plastic, beam with free ends, including the effects of rotatory inertia and moment–shear interaction. At early times the plastic shear strain rate γ_t^p in region I is dominant; at later times γ_t^p becomes negligibly small and the plastic curvature rate κ_t^p is dominant. Thus, region I is initially a plastic shear hinge and subsequently becomes a plastic bending hinge. This behavior is analogous to that reported in [25].

Figure 20 shows the distribution of plastic strain along the length of the beam for $V_0 = 500$ in./sec at $t = 94\,\mu$sec. For x in the interval (3·5, 4 in.), which corresponds to region III of Fig. 19, the plastic strain is negligibly small. Thus, the plastic zone, region III, which is not predicted by the rigid plastic theories [12, 25] is a region of extremely small plastic strains.

One aspect of the loading surface which perhaps warrants further study is the hardening model which is employed. Examination of the elastic–plastic boundaries in Fig. 19 shows that some segments of the beam experience plastic flow associated with both positive and
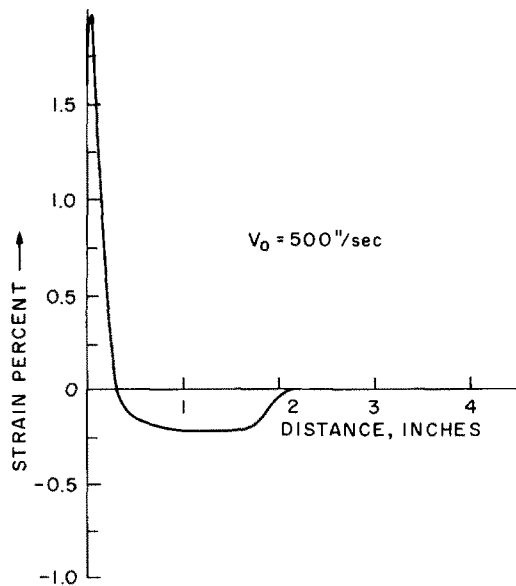

Fig. 20. Plastic strain at $t = 94\,\mu$sec.

negative moments. This suggests that inclusion of a Bauschinger effect in the analysis might be important. Use of a "kinematic" hardening model which incorporates this effect should clarify the situation.

7. CONCLUDING REMARKS

The ratio of the energy dissipated in plastic deformation to the total energy supplied to the beam is a measure of the extent of plastic deformation in the beam. Numerical results for high velocity impact tests indicate that over 40 per cent of the energy is converted into plastic work while less than 5 per cent is stored as elastic strain energy. Kinetic energy accounts for the remaining part. These figures suggest that material behavior for plastic flow should be important in predicting strain–time profiles and that the qualitative agreement between the computed profiles and those observed in the experiments indicates that the model used in substantially correct. However, the experiments are not sensitive enough to the model used for plastic flow to allow conclusions regarding the details of the constitutive equations to be used for describing plastic behavior. For example, the experiments do not appear to be sensitive enough to determine the increase in flow stress due to strain rate effects which for the aluminum alloy used here is expected to be less than 20 per cent. Thus the experiments and the analysis indicate the nature of the structural response associated with plastic bending waves but do not give definitive information regarding the material behavior during plastic flow. The qualitative agreement between the experimental strain response and the theoretical predictions indicates that the analysis presented here provides a reasonably good description of the dynamic response of aluminum beams to impact loading. The plastic regions according to the present theory are shown to correspond roughly to the fixed and moving plastic hinges of Conroy's solution based on rigid perfectly plastic beam theory. The deflected shapes predicted by the two theories were also found to be similar. Thus, although the presence of work hardening in the theory used here precludes a definitive comparison of this theory with the simpler rigid plastic theory, it appears that the latter theory is suitable for predicting the main features of the beam response.

The principal discrepancy between the strain–time profiles obtained from the experiment and those predicted by the theory is the large upward shift of the predicted strain–time profile at stations near the point of load application, such as shown in Fig. 7 for $x = \frac{1}{2}$ in. As mentioned previously this discrepancy may be partly due to poor matching of the slopes of the empirical moment–curvature curve with those of the experimental curve. Another reason for this discrepancy appears to be that the station $x = \frac{1}{2}$ in. is too close to the point of impact for the results of beam theory to be valid. The wave propagation phenomenon near the point of application of the load is complicated by the presence of plastic loading waves and elastic unloading waves from reflections at the free surfaces. Plastic waves being considerably slower than elastic waves suggests that more time would be required for a sufficient number of reflections to take place for beam theory to become a good approximation. Also faster elastic unloading waves would tend to overtake the leading plastic loading waves and reduce the amplitude of the peak strain which occurs at $t = 15\ \mu\text{sec}$ for $x = \frac{1}{2}$ in. It is doubtful that these complicated effects can be modeled by an elastic–plastic beam theory at distances less than three beam thicknesses from the point of impact. In the elastic region following the first strain peak the change in strain according to the

theory is very similar to that observed in the experiments. Thus it appears that the theory over-estimates the early plastic strain peak and that this error in plastic strain is not recovered in the subsequent elastic response.

REFERENCES

[1] E. W. PARKES. Permanent deformation of a cantilever struck transversely at its tip. *Proc. R. Soc.* **A228**, 462–476 (1955).
[2] E. W. PARKES, Some simple experiments on the dynamic plastic behavior of mild steel beams. *Br. Welding Jl* **3**, 362–366 (1956).
[3] E. W. PARKES. Permanent deformation of an encastre beam struck transversely at any point in its span. *Proc. Instn. Civ. Engrs* **10**, 277–304 (1958).
[4] S. R. BODNER and P. S. SYMONDS. Plastic Deformations in Impact and Impulsive Loading of Beams, pp. 488–500; Plasticity, *Proc. II Symposium on Naval Struct. Mech.*, edited by E. H. LEE and P. S. SYMONDS (1960).
[5] S. R. BODNER and P. S. SYMONDS, Experimental and theoretical investigation of the plastic deformation of cantilever beams subjected to impulsive loading. *J. appl. Mech.* **29**, 719–727 (1962).
[6] A. L. FLORENCE and R. D. FIRTH, Rigid plastic beams under uniformly distributed impulses. *J. appl. Mech.* **32**, 481–488 (1965).
[7] D. L. HOLT, S. G. BABCOCK, S. J. GREEN and C. J. MAIDEN. Strain rate dependence of the flow stress in some aluminum alloys. *Trans. Am. Soc. Metals* **60**, 152 (1967).
[8] P. S. SYMONDS. Survey of Methods of Analysis for Plastic Deformation of Structures Under Dynamic Loading, Brown University Report (1967).
[9] P. S. SYMONDS, Survey of Progress in Plastic Wave Propagation in Solid Bodies, Brown University Report (1967).
[10] P. E. DUWEZ, P. S. CLARK and H. F. BOHNENBLUST, Behavior of long beams under impact loading. *J. appl. Mech.* **17**, 27–34 (1950).
[11] I. VIGNESS. Propagation of Transverse Waves in Beams, Report F-3476, Naval Research Laboratory (1949).
[12] M. F. CONROY. Plastic-rigid analysis of long beams under transverse impact loading. *J. appl. Mech.* **19**, 465–470 (1952).
[13] T. R. WILSHAW and J. M. KELLY. Response of circular clamped plates to square wave stress pulses. *Exp. Mech.* **8**, 450–458 (1968).
[14] S. RANGANATH, Normal Impact of an Infinite Elastic Beam by a Semi-Infinite Elastic Rod, Brown University Report ARPA E69 (1969).
[15] S. RANGANATH, Normal impact of an infinite elastic beam by a semi-infinite elastic rod. *J. appl. Mech.* **38**, 455–460 (1971).
[16] D. C. DRUCKER, Effect of shear on the plastic bending of beams. *J. appl. Mech.* **23**, 509–514 (1956).
[17] D. C. DRUCKER, More Fundamental Approach to Plastic Stress Strain Relations, *Proc. First U.S. Nat. Congr. Appl. Mech.*, p. 487. ASME (1951).
[18] R. J. CLIFTON, An Analysis of Combined Longitudinal and Torsional Plastic Waves in a Thin Walled Tube, *Proc. 5th U.S. Nat. Congr. Appl. Mech.*, pp. 465–480. Univ. of Minnesota (1966).
[19] R. COURANT and D. HILBERT. *Methods of Mathematical Physics*. Vol. 2. Interscience (1962).
[20] R. COURANT, E. ISAACSON and M. REES, On the solution of non-linear hyperbolic differential equations by finite differences. *Communs pure appl. Math.* **5**, 243–255 (1952).
[21] S. RANGANATH and R. J. CLIFTON, A Second Order Accurate Difference Method for Systems of Hyperbolic Partial Differential Equations, Technical Report No. 2 under Contract No. F33615-70-C-1101 with Brown University (1971).
[22] R. COURANT, K. O. FRIEDRICHS and H. LEWY, Uber die partiellen differenzengleichungen der mathematischen Physik. *Math. Ann.* **100**, 32–74 (1928).
[23] *Aluminum*. Vol. 1, p. 306. ASM (1967).
[24] J. BEJDA, A solution of the wave problem for elastic–viscoplastic beams. *J. Méc.* **6**, 263–282 (1962).
[25] B. KARUNES and E. T. ONAT. On the effect of shear on plastic deformation of beams under transverse impact loading. *J. appl. Mech.* **27**, 107 (1960).

Абстракт—Получаются решени для задачи нормального удара в бесконечную упруго—пластическую балку посредством полубесконечнош упругояо стержн. Учитываются эффекты инерции вращения и деформации сдвига, в определяющих уравнениях движения балки. Для описания поведения материала, используется модель, независимая от скорости деформации и основанная на понятиях, похожих на применяемых в квезистапической пластичности. Учитывается взаимодействие между моментом и силой сдвига. Используется критерий упрочнения деформации, основанный на квазистатической зависимости момент-кривизна для чистого изгиба. Характер деформации во времени, подсчитан при использовании зтой теории, сходится надлежчщим образом, с результатами полученными из зкспер’ментов на алюминиевых балках. Затем, сравниваются решения с предпосылками, основанными на теории балок, в рамках, идеальной жесткой пластипности.